Estimation of the 2002 Mount Etna eruption cloud radiative forcing from Meteosat-7 data

C. Bertrand*, N. Clerbaux, A. Ipe, L. Gonzalez

Department of Observations, Section Remote Sensing from Space, Royal Meteorological Institute of Belgium, Avenue Circulaire 3, B-1180 Brussels, Belgium

Abstract

On 27th October 2002, after 15 months of small activity, the Mount Etna located on the island of Sicily, Italy (37.73 °N, 15.00 °E) erupted undergoing one of its most vigorous eruptions in years. During a few days, Europe's highest and most active volcano hurled lava and spewed significant amounts of ash and trace gases into the atmosphere. The smoke and ash plume originating from the volcano stretched from the Sicily to the north African coast.

The plume from the volcano has been identified and tracked using half-hourly Meteosat-7 visible, infrared, and water vapor imagery in order to estimate the radiative forcing produced by the introduction of the volcanic cloud in a previously clear sky. Our results indicate that, while the volcanic cloud has introduced a well-discernable radiative perturbation, the magnitude of the shortwave volcanic forcing appears in the range of the one introduced by large clouds above the Mediterranean Sea. By contrast, the perturbation generated in the longwave spectrum at the top of the atmosphere is larger than the one introduced by large meteorological clouds.
© 2003 Elsevier Inc. All rights reserved.

1. Introduction

Located on the island of Sicily (see Fig. 1), Mount Etna is one of the most studied volcanoes on Earth. This volcano is known to almost constantly rumble with its fissures acting like vents, releasing pressure at regular intervals instead of allowing it to build up into a massive explosion. Etna had not produced any serious activity since a series of eruptions in July and August 2001. On the early morning of 27 October 2002, a new flank eruption began at Etna. The eruption was very visible even at greater distance, such as the Aeolian Islands, more than 100 km to the north. After its extremely vigorous start, the eruption showed a declining trend through 5 November and then continued in a more or less stable manner, finally ending on 28 January 2003.

The 2002 eruption was one of the most explosive eruptions of this volcano in recent times. More than two-thirds of the total volume of erupted products were pyroclastic, contrasting with most recent eruptions of Etna which produced mainly (or nearly exclusively) lava. Explosive eruptions inject enormous volumes of volcanic ash and gases into the atmosphere, where the ash is carried downwind hundreds or thousands of kilometers. The larger volcanic ash particles are expected to settle out in a short period of time, but the sulphuric acid aerosols produced by the emitted sulphur-rich gases will persist for several years (e.g., Rampino & Self, 1984; Robock & Mao, 1995).

These aerosols will impact the Earth's energy budget (see, e.g., Hansen, Wang, & Lacis, 1978; Stenchikov et al., 1998) both regionally (for the few months following the eruption when the aerosol cloud is inhomogeneous) and on a global scale (in less than a year the cloud becomes fairly uniformly distributed and produces no discernible regional forcing) (Robock & Matson, 1983). The long-lasting effect of a volcanic eruption is mainly due to the sulphur content of the emissions that reach the stratosphere. The sulphur gases convert into small sulphate droplets, which are distributed over the globe and effectively scatter the solar radiation. Normally, this long-lasting aerosol is the focus of investigations of the role of volcanism in climate change and variability (see, e.g., Bertrand, van Ypersele, & Berger, 1999, 2002). In the case of strong and explosive eruptions,

* Corresponding author. Tel.: +32-2-3730615; fax: +32-2-3746788.
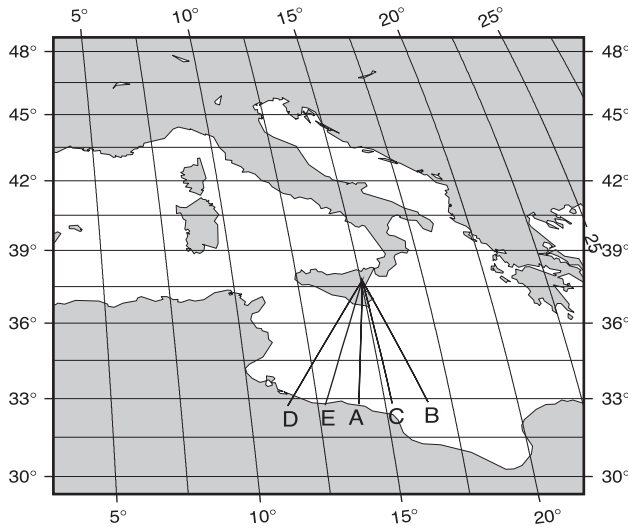*E-mail address:* Cedric.Bertrand@oma.be (C. Bertrand).

Fig. 1. Definition of the volcanic cloud tracking zone. Upper left corner located at 47.58°N, 3.75°E; upper right corner at 48.70°N, 29.22°E; lower left corner at 29.34°N, 2.81°E; and finally the lower right corner at 29.72°N, 20.91°E. Also displayed are the five (A to E) sections starting from the Etna location and crossing the Mediterranean Sea for which TOA radiative perturbations are provided Figs. 4–8.

however, there is also an extensive production of silicate aerosols. Depending on the proportion, this is removed from the atmosphere within 1–3 or 4 months by dry fall-out, wash-out, and rain-out. These non-sulphuric aerosols, at least regionally, can produce optical depths exceeding those of the sulphuric aerosols by an order of magnitude or more (e.g., Hirono, Shibata, & Fujiwara, 1985). Thus, the question arises, what impact does the volcanic eruption cloud (consisting of a mixture of silicate particles-ash and the larger lapilli, volcanic and environmental gases, and condensed water) exercise on the radiative fluxes.

Regarding the 2002 Mount Etna eruption, dense ash clouds and gaseous emissions were detected by several space-borne sensors: the Medium Resolution Imaging Spectrometer (MERIS) onboard ESA's Envisat satellite, the Global Ozone Monitoring Experiment (GOME) sensor and the Along Track Scanning Radiometer ASTR-2 onboard the ESA's ERS-2 spacecraft, the Moderate Resolution Imaging Spectroradiometer (MODIS) instrument on NASA's Terra and Aqua satellites. At dawn on 27 October, an enormous black cloud rose several kilometers above the vents on the upper southern flank, while smaller ash columns rose from the vents on the northeast Rift. The plume was driven southward over the densely populated areas around Catania, causing heavy ash falls that paralyzed public life and traffic for several days. In this paper, we estimate the radiative forcing seeds introduced by Etna's volcanic cloud into a previously clear sky. Indeed, volcanic ash contains black graphite and carbon particles which are dark, thus absorb sunlight. As these atmospheric particles reduce the amount of sunlight reaching the planet's surface, they increase the amount of solar energy absorbed in the

atmosphere, thus simultaneously cooling the surface and warming the atmosphere. Taking advantage of the high temporal sampling of the eruptive zone afforded by the geostationary orbit, we used the half-hourly Meteosat-7 visible, infrared, and water vapor imagery to identify, track, and finally estimate the radiative forcing operated by the volcanic cloud during the first 4 days (from October 27 to 30) when eruption was the most vigorous.

This paper is subdivided as follows: First, we describe how the outgoing longwave radiation (OLR) and outgoing shortwave radiation (OSR) were retrieved from Meteosat-7 data. Next, eruption cloud detection and tracking are presented. Then, the method of radiative forcing by the volcanic cloud is presented and discussed. Finally, we present some limitations of our method and provide a prospective for its use at other locations.

2. Derivation of the top of the atmosphere radiative fluxes

This section describes the system that has been implemented at Royal Meteorological Institute of Belgium (RMIB) and is routinely used to estimate the top of the atmosphere (TOA) radiative fluxes from the Meteosat-7 data. Table 1 provides the accuracy budget of the resulting shortwave and longwave TOA fluxes.

2.1. Meteosat instrument calibration

When estimating the radiative fluxes at the TOA, the prime instrumental characteristics of importance are the spectral response function(s) and the radiometric calibration(s) of its channels. Indeed, any calibration error will propagate through the processing up to the final products. The Meteosat-7 infrared (10.5–12.5 μm) and water vapor (5.7–7.1 μm) channels are calibrated using an absolute calibration, based on the on-board black body calibration technique. The mechanism uses two black bodies with known temperatures, which can be viewed sequentially: one having the ambient spacecraft temperature and one heated to about 50 K above it. This method allows a calibration of the measurements estimated as better than 2 K in equivalent brightness temperature. On the other hand, EUMETSAT only provides a raw estimate of the visible

Table 1
Summary of the error magnitudes associated to the TOA flux estimation from Meteosat-7 measurements

Steps	Shortwave (%)	Longwave (%)
Narrow band measurement	5	1
NB-to-BB conversion	5.5	1.5
Radiance-to-flux conversion	6	2
Total	16.5	4.5

Note that these magnitudes have to be understood as typical accuracies since they are function of the viewing geometry.

channel (0.45–1.0 μm) calibration. To overcome this weakness, a cross-calibration of the Meteosat-7 visible channel has been performed (Clerbaux, 2002) according to the well-calibrated shortwave channel of the CERES instrument on the TRMM and Terra spacecrafts (Wielicki et al., 1996).

2.2. Retrieval of outgoing longwave radiation

Meteosat does not measure the total quantity of energy reaching the instrument but only the energy in its three spectral channels. For this reason, the estimation of the outgoing longwave radiative flux (OLR) over the entire longwave spectrum from radiance observations made in narrow spectral bands requires what is often referred to a narrowband-to-broadband (NB-to-BB) conversion. This aims to estimate the total longwave radiance, L_{lw}, from the water vapor, L_{wv}, and infrared, L_{ir}, filtered measurements of Meteosat-7. According to Schmetz and Liu (1988), this conversion is conveniently performed using polynomial regressions. Regarding the Meteosat case, we use a second order regression model:

$$\widetilde{L_{lw}} = C_o(\theta_v) + C_1(\theta_v) + C_2(\theta_v)L_{ir} + C_3(\theta_v)L_{wv}^2$$
$$+ C_4(\theta_v)L_{wv}L_{ir} + C_5(\theta_v)L_{ir}^2 \quad (1)$$

where, due to the limb-darkening, the regression coefficients, C_i ($i = 0,...,5$), are dependent on the viewing zenith angle, θ_v. Those coefficients are determined by root mean square error minimization over a large data base of spectral radiance curves, $L(\lambda)$, at the TOA.[1] As described in Clerbaux et al. (2003), the data base has been generated using the Santa Barbara DISORT Atmospheric Radiative Transfer (SBDART) code (Richiazzi, Yang, Gautier, & Sowle, 1998) for 4620 different conditions for the Earth–atmosphere system. The error introduced by the narrowband-to-broadband conversion is estimated as the root mean square difference between the estimated, $\widetilde{L_{lw}}$, and actual, L_{lw}, longwave radiances normalized by the averaged radiance, $\langle L_{lw} \rangle$, to get relative error in (%):

$$\epsilon = \frac{1}{\langle L_{lw} \rangle} \sqrt{\frac{1}{N} \sum_{1}^{N} (\widetilde{L_{lw}} - L_{lw})^2} \quad (2)$$

The parameterization of Eq. (1) by Dewitte and Clerbaux (1999) leads to a NB-to-BB error of $\epsilon = 1.5\%$.

Following the NB-to-BB conversion, the broadband flux, F, is estimated from the directional broadband radiance, $L(\theta,\phi)$, using a model, $R(\theta,\phi)$, of the radiance field at the TOA:

$$R(\theta,\phi) = \frac{\pi L(\theta,\phi)}{F} \quad (3)$$

that corresponds to the ratio between the radiance emitted in the direction (θ,ϕ) and the equivalent Lambertian radiance (F/π). When the angular distribution of the energy $R(\theta,\phi)$ is known, the flux can be inferred from the radiance as:

$$F = \frac{\pi L(\theta,\phi)}{R(\theta,\phi)} \quad (4)$$

Because the thermal angular conversion of the radiance field is, in average, not dependent on the azimuth angle of observation, ϕ, the angular model, $R(\theta,\phi)$, reduces to $R(\theta)$, which now represents the limb-darkening and is mainly dependent on the atmospheric profiles of temperature and humidity and on the possible cloud cover. Clerbaux et al. (2003) provides a comprehensive description of the angular dependency models (ADMs) that were used for the thermal flux retrieval. As for thermal radiation, the flux inference from radiance does not need an explicit scene identification, the ADM is obtained by spectral analysis of the NB radiances of the imager ("implicit identification"). We quantified the error introduced by the radiance-to-flux conversion to $\epsilon = 2\%$, in average.

2.3. Retrieval of reflected solar radiation

As for the OLR, the determination of the OSR starts with a NB-to-BB radiance conversion. In this first step, the total shortwave radiance is estimated from the visible filtered measurements using a third order regression on the filtered measurements:

$$L_{sw} = D_0(\theta_s) + D_1(\theta_s)L_{vis} + D_2(\theta_s)L_{vis}^2 + D_3(\theta_s)L_{vis}^3 \quad (5)$$

where the regression coefficients D_i ($i = 0,...,3$) depend on the solar zenith angle, θ_s. Eq. (5) can be seen as a kind of implicit scene identification based on the reflectance in the visible band. This explains why the coefficients are dependent on the illumination and then on the solar zenith angle, θ_s. In this equation, the NB-to-BB conversion coefficients are neither dependent on the viewing zenith angle nor on the azimuth angle because the radiative transfer (RT) model used to generate the spectral radiance data base supposes Lambertian surface reflectances. This makes sense because the spectral signature of a scene does not change significantly according to the direction of observation.

As for the longwave, the coefficients in Eq. (5) are obtained by least mean square minimization on the database of spectral radiance curves. Albeit a second order regression was sufficient for the longwave, a third order regression has proved to be the best choice for the shortwave. The error introduced during the shortwave NB-to-BB conversion is estimated to $\epsilon = 5.5\%$, which is worse than for the longwave. This is explained by the fact that there is only one shortwave channel on Meteosat (two in the thermal range) and also by the higher dispersion in

---

[1] The database as well as the related documentation are available at: http://gerb.oma.be/SpectralRadiancesDB.

spectral signature, $L(\lambda)$, in the shortwave part of the spectrum due to the infinite possibility of spectral reflectance, $\rho(\lambda)$, according to the surface type.

By contrast to the NB-to-BB radiance conversion, our BB radiance-to-flux conversion accounts for the non-isotropic distribution of the radiance. Because most natural surfaces are non-Lambertian, we make use of ADMs to perform the angular integration. Scenes exhibiting a close angular distribution of the energy can be merged together to form a set of ADMs (Loeb et al., 2003). A set of 590 shortwave ADMs for TOA radiative flux estimation has been recently derived by Loeb et al. (2003) from a statistical analysis of measurements of the CERES instrument onboard of the NASA's TRMM satellite. For clear scenes, CERES/TRMM SW ADMs are defined over ocean, land, and desert, while theoretical ADMs are used over snow. Over land, ADMs are divided into two classes: moderate-to-high tree/shrub coverage and low to moderate tree/shrub coverage. Desert ADMs are defined for dark and bright desert regions. ADMs for cloudy conditions are defined for several classes stratified by surface type, cloud fraction, cloud phase, and cloud optical depth.

The conversion of one Meteosat-7 footprint BB radiance into the corresponding flux requires therefore a scene identification to properly select the adequate ADM among the set of 590 ADMs. This needs the characterization of the surface type and the cloud properties within the footprint. In practice, the Global Land Cover Map (v1.2) produced by the International Geosphere Biosphere Programme (IGBP) (Belward, 1996; Belward, Estes, & Kline, 1999) has been used to associate one of the six CERES-TRMM class to each Meteosat-7 pixels. This was done by merging the 17 IGBP surface types into the CERES-TRMM surface types. Note that except for snow, the Meteosat-7 pixel registration according to the CERES-TRMM classes is taken invariant in time. The characterization of the cloud cover in term of cloud fraction within the footprint, cloud optical thickness, and cloud phase is provided by our cloud-screening algorithm. This simple algorithm (see detail in Appendix A) has been built in order to provide cloud property retrieval as close as possible to the CERES cloud retrieval (Minnis et al., 1995) (to minimize errors in the ADM selection process).

As we see, by using the CERES/TRMM SW ADMs, the surface reflectance anisotropy is implicitly taken into account in our TOA flux retrieval because all the surface considerations (BRDF and surface albedo) have been taken into account by Loeb et al. (2003) when derivating their angular distribution models for top of the atmosphere radiative flux estimation. Nevertheless, it is worth pointing out that the ADMs derived by Loeb and colleagues have to be view for a given class as the mean state/behaviour of this particular class. This can therefore introduce some limitation in our fluxes retrieval for at least two distinct reasons but explain why our pixels

registration is taken as invariant in time (excepted for snow). First, vegetation phenology changes from spring to spring over 12-month cycle, which therefore impact on the associated radiance field. Second, even if a surface type do not change, its reflectance (radiance) is allowed to vary depending on whether it is wet or dry. Note that, in the present study, the ash from the Mount Etna volcano has traveled mostly over the ocean for which these two cases do not apply.

3. Identification of the volcanic plume and eruption cloud tracking

Airborne volcanic ash from violent eruptions can cause a range of damage to airplanes that fly through an eruption cloud (Pieri et al., 2002; Rose, 1986) and volcanic cloud encounters by aircraft have become more common in recent years (Casadevall, 1994; Casadevall & Krohn, 1995). Such dangerous and costly encounters can happen because ash clouds are difficult to distinguish from ordinary clouds, both visually and on radar. Detecting explosive volcanic eruptions and locating the eruption cloud is thus crucial to aviation safety. Operational detection and tracking of volcanic ash has relied heavily on a split window differencing technique of thermal longwave infrared channels on currently operational satellites. As an example, the brightness temperature difference from the Advanced Very High Resolution Radiometer (AVHRR) band 4 (10.3–11.3 μm) minus band 5 (11.5–12.5 μm) (or equivalent, i.e., the difference between the 11 and 12 μm MODIS bands) are used to detect and track the volcanic cloud since volcanic plume are known to have a negative [2] ΔT $(= T_4 - T_5)$ (e.g., Prata, 1989; Wen & Rose, 1994), while meteorological clouds generally have positive brightness temperature differences [3] (Yamanouchi, Suzuki, & Kawaguchi, 1989). The magnitude of the negative brightness temperature difference for volcanic clouds is dependent upon the optical thickness of the cloud, the amounts of water, volcanic ash and sulfuric acid in the cloud, the size distribution of the particles in the cloud, and the temperature contrast between the cloud and the underlying surface (i.e., meteorological clouds, land, or water) (Prata, 1989; Wen & Rose, 1994).

However, as highlighted by Simpson, Hufford, et al. (2000), there are multiple failure modes in the technique of Prata (1989) and Schneider, Rose, and Kelley (1995).

---

[2] For transparent volcanic clouds, the absorption of energy from the underlying surface is greater in the band 4 region than the band 5 region, due to a larger refractive index for silicates in the band 4 region than in the band 5 region.

[3] For meteorological clouds, the absorption of the energy from the underlying surface is greater in band 5 than in band 4, due to a larger refractive indices for water and ice particles in the band 5 region than in the band 4 region.

As an example, during the initial phase of the eruption, the $T_4 - T_5$ volcanic ash detection method is generally inoperative because volcanic plume imaged at that time is optically thick making its spectral signal very much like a meteorological cloud. Indeed, for opaque volcanic and meteorological clouds, all the emitted thermal energy from the surface underlying the cloud is absorbed by the cloud. The radiance recorded by the satellite sensor is only that which is emitted by the cloud. At typical cloud temperatures, the band 4 radiance is greater than the band 5 radiance, which results in a positive band 4 minus 5 brightness temperature difference. As the volcanic cloud disperses and becomes more translucent, the spectral properties of the cloud change, producing a volcanic cloud signal that can then be distinguished using the brightness temperature difference approach and detection becomes more likely. Eventually, the concentration gradient becomes very small and detection is lost.

Due to the design of the Meteosat sensor (i.e., only one infrared thermal channel), use of the split window technique is not possible. Therefore, rather than using the magnitude and the sign of the brightness temperature difference, we based our volcanic cloud detection and tracking on a thermal radiance anomaly procedure. Namely, besides the 192 directional thermal radiance images, we operationally computed from October 27 at 00:00 UTC to October 30 at 23:30 UTC, using the half-hourly Meteosat-7 water-vapor and infrared records as previously described, we estimated 48 (one for each half-hourly Meteosat-7 scene over a day) clear-sky directional emitted thermal radiance images. Then,
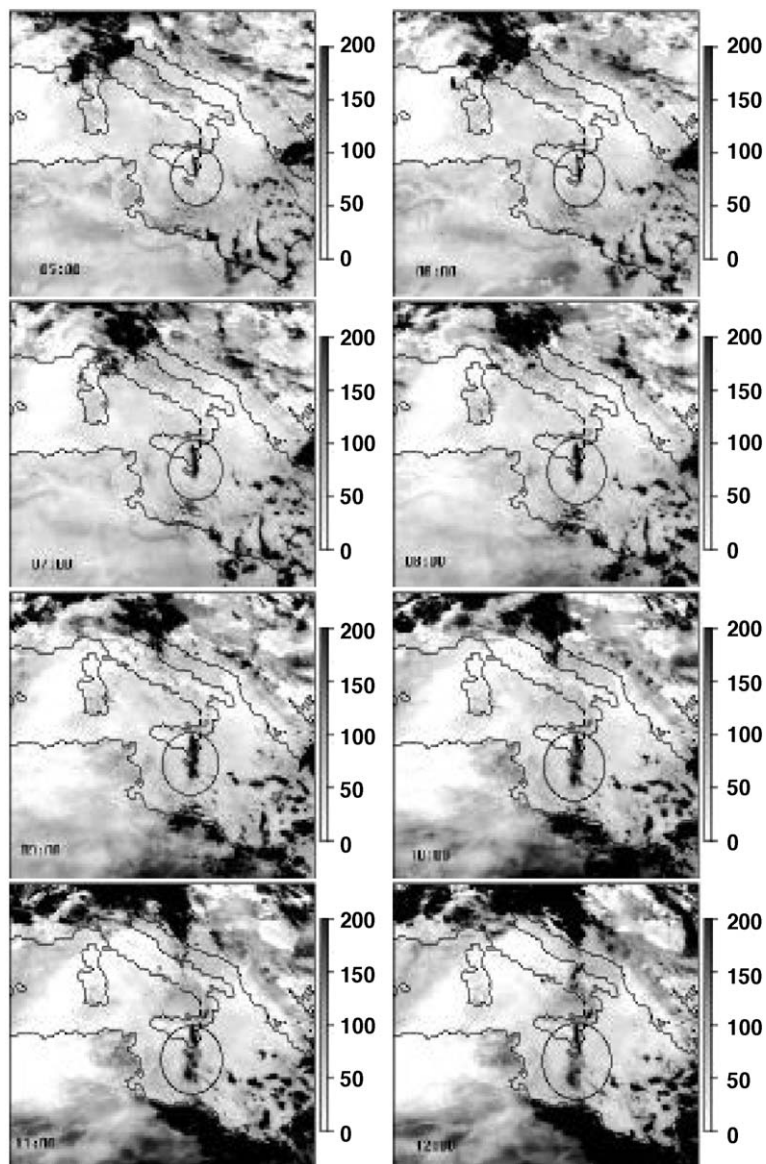

Fig. 2. Unfiltered thermal radiance anomaly at respectively, 5:00, 6:00, 7:00, 8:00, 9:00, 10:00, 11:00 and 12:00 UTC on October 27, 2002. Units are given in 0.05 W m^{-2} sr^{-1}.

by subtracting for each time stop the computed unfiltered thermal radiance from the clear-sky one, the visibility of the eruption cloud is significantly enhanced. When combined with the high temporal sampling of Meteosat, it is possible, by following the volcanic cloud time step by time step, to discriminate it from meteorological clouds. In order to minimize the impact of clouds, a compositing technique over a period of 14 days is applied to retrieve the unfiltered clear-sky thermal radiance images. For each scene, s, the clear-sky thermal radiance image, L_{clr}, is built by selecting the highest thermal radiance computed for the given scene, s_x, and for each pixel, p, in the image over the time period of 14 days.

$$\forall \; s_x \in s, \; (x = 1, \; 48) \quad L_{clr}(s_x, p) = \text{Max}[L(d_i, s_x, p)]$$
$$(i = 1 \text{ to } 14) \tag{6}$$

Note that, although the compositing process effectively removes cloud-obscured observations and reduces the effects of variable atmospheric attenuation (Holben, 1986), one limitation of this approach is that if more than one clear measurement occurs during the compositing period then the technique will still select the "clearest". In the case of vegetation indices compositing, this can lead to not preserving the vegetation information; compositing, for example, may bias observation of the precise timing in foliar changes through the growing season. This is less important here because our purpose is to prepare a temporal series of images in order to map the volcanic cloud and not quantify the magnitude of the directional thermal radiance anomaly.

The evolution of the volcanic cloud signal as provided by the thermal radiance anomaly method can be seen in the series of images (in central part of these images) in Fig. 2 illustrating the volcanic cloud evolution and dispersion few time after the beginning of the Etna eruption on October 27. In addition, an animation (available at ftp://gerb.oma.be/cedric/Rad_D.gif) displays the time evolution of the unfiltered thermal radiance anomalies from October 27 00:00 UTC to October 30 23:00 UTC using data sampled at 1-h interval (units in the animation are given in 0.05 W m^{-2} sr^{-1}). As highlighted by this animation, while the eruption progressed, smoke and ash drifted toward the African coast from Mount Etna caught first by low-level winds blowing to the southeast and to the south toward Africa at higher altitudes.

4. Etna eruption cloud radiative forcing (ECRF)

By analogy with the concept of cloud radiative forcing (CRF) at the top of the atmosphere, which is a measure of the impact of clouds on the energy balance of the Earth and represents the change in net radiation associated with clouds (Hartmann, Moy, & Fu, 2001), we introduce the concept of

ECRF. From the CRF definition of Ramanathan et al. (1989), we can define the longwave eruption cloud radiative forcing (LWECRF) as being the difference between the volcanic cloudy sky and clear-sky longwave radiative flux at the TOA:

$$LWECRF = FN_{lw} - FN_{lw}(clr) \tag{7}$$

where FN_{lw} is the net volcanic cloudy sky longwave radiative flux at the top of the atmosphere and $FN_{lw}(clr)$ the net clear-sky longwave radiative flux at the top of the atmosphere. The shortwave volcanic cloud radiative forcing (SWECRF) is then calculated as:

$$SWECRF = S(\alpha_{clr} - \alpha) \tag{8}$$

where S is the mean incoming solar flux, α_{clr} the TOA clear-sky albedo, and α the eruption cloud albedo at the TOA. Finally, the net TOA eruption cloud radiative forcing is computed as the difference of the net radiative fluxes between volcanic cloudy sky and clear sky at the TOA
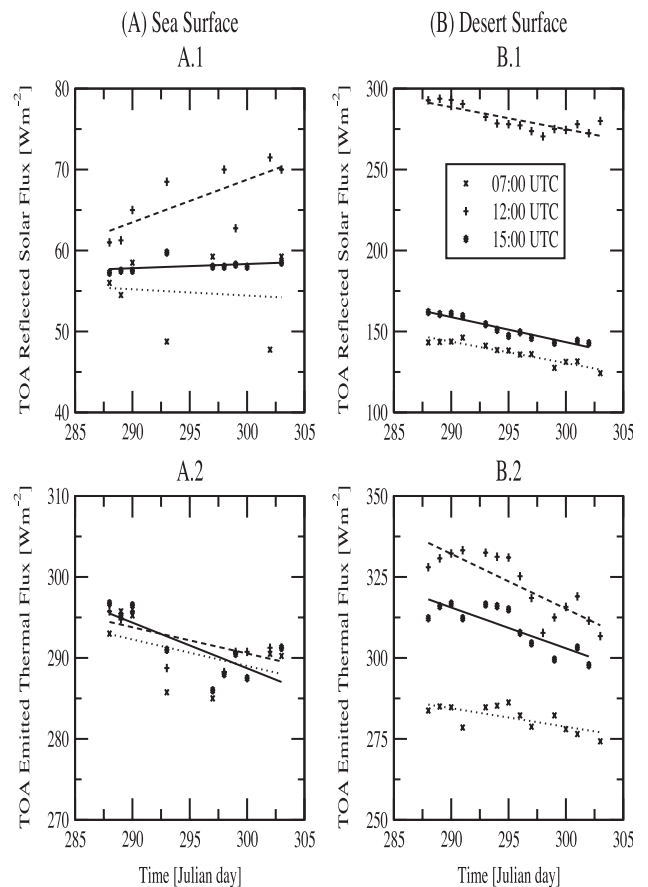

Fig. 3. Unforced TOA reflected solar (1) and emitted thermal (2) radiative fluxes daily variations as estimated for a given pixel over (A) a sea surface and (B) a desert surface. Dotted lines represent the linear regression fit applied to the 07:00 UTC (×) data, dashed lines the regression fit relative to the 12:00 UTC (+) data, and finally, the solid lines the regression fit associated to the 15:00 UTC (★) data.

(e.g., the sum of the longwave and shortwave radiative forcing):

$$NETECRF = LWECRF + SWECRF \qquad (9)$$

The NETECRF can be expressed in term of incident solar radiation, S, reflected solar radiation at the TOA, OSR, and OLR as follows:

$$NETECRF = (S - OSR - OLR) - (S_{clr} - OSR_{clr} - OLR_{clr}) \qquad (10)$$

where the suffix "clr" refers to clear-sky fluxes (e.g., radiative fluxes that are not contaminated by volcanic and meteorological clouds). Because the value of the incident solar radiation at TOA is independent of the presence or absence of clouds in the Earth's atmosphere, the NETECRF reduces to the following estimation:

$$NETECRF = (OSR_{clr} - OSR) + (OLR_{clr} - OLR) \qquad (11)$$

In this equation, the term $(OSR_{clr} - OSR)$ accounts for the SWECRF and the term $(OLR_{clr} - OLR)$ provides the LWECRF. As for the CRF, the values of eruption cloud forcing are negative for a cooling effect with respect to clear sky and positive for a warming effect.

4.1. Reference clear-sky determination of fluxes

Once the volcanic plume is identified and signposted throughout the time and area of interest, estimation of the radiative perturbation produced by the volcanic cloud
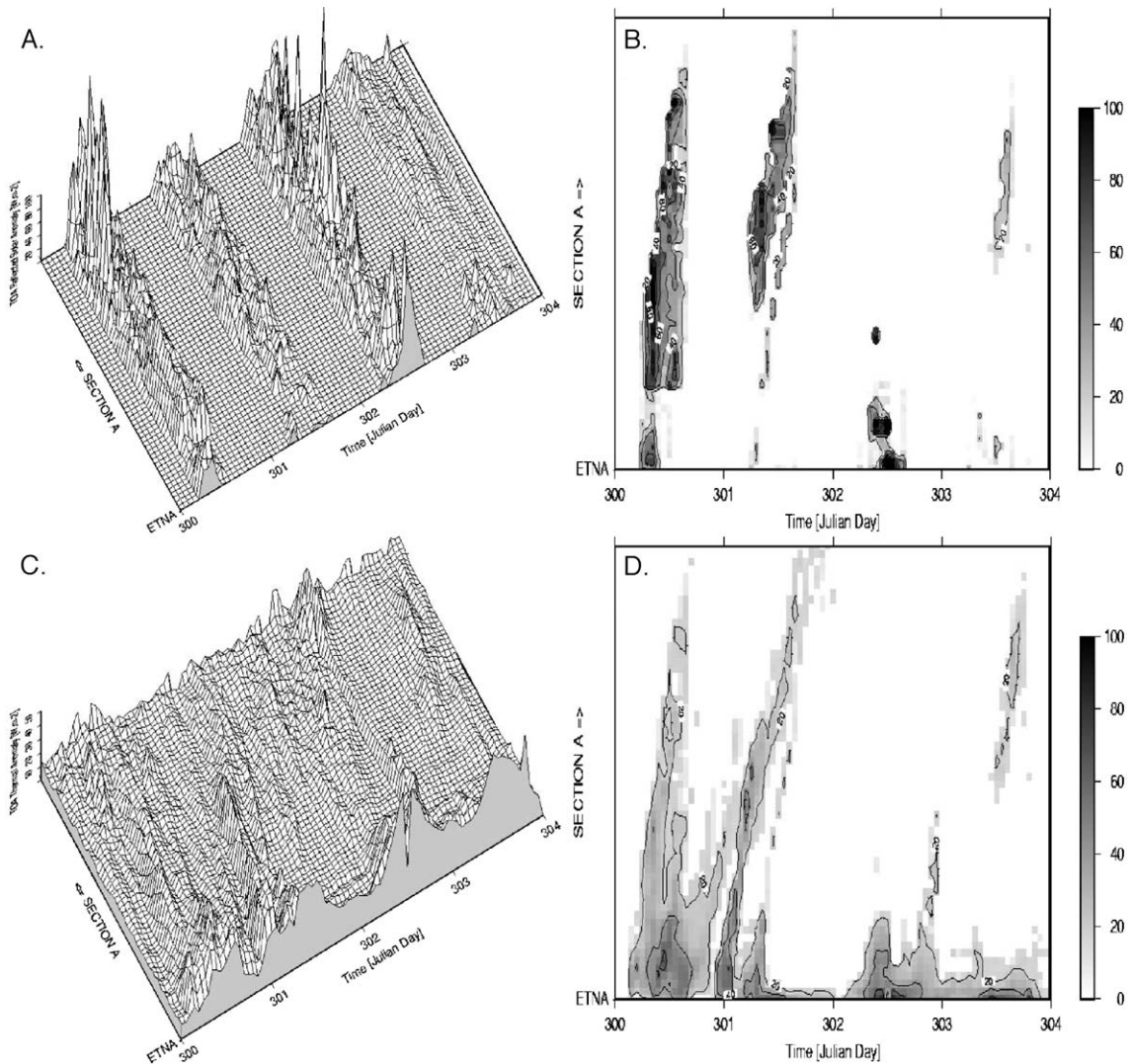

Fig. 4. Radiative perturbations along the section A (from the Etna location to 32.78 °N, 14.01 °E). Panels A and C provide, respectively, the anomalies in the reflected solar flux and emitted thermal radiation at the TOA from October 27 to October 30 with respect to a reference clear sky situation, while panels B and D only display the radiative forcings related to the Etna eruption cloud. The SW forcing is a negative radiative forcing while, the LW forcing is positive. Units are given in W m^{-2}.

requires determination of a series of reference short- and longwave clear-sky fluxes, from which radiative anomalies are computed (see Eq. (11)). As for the unfiltered clear-sky thermal radiances, a compositing technique is used to generate these reference clear-sky fluxes. However, while a slight overestimation/underestimation in the clear-sky thermal radiance does not really impact on the volcanic cloud detection, the volcanic forcing quantification requires a larger accuracy when estimating the clear-sky fluxes. Indeed, as shown in Fig. 3, clear-sky fluxes exhibit daily variation. This figure provides the time evolution of both clear-sky OSR and OLR at TOA for two different surface types (sea and desert) inside our domain of interest and for three Meteosat-7 scenes (respectively at 07:00, 12:00, and 15:00 UTC). As it can be seen, the net clear-sky "unforced" TOA reflected solar flux variations over a time period of 15 days can reach up to 20 W

m^{-2} over a desert surface and up to 10 W m^{-2} over a sea surface in our domain. Note that the magnitude and the sign (positive or negative) of the variation in the reflected solar flux over sea surface are largely function of the scene reference time and the pixel geolocation. Indeed, while over a desert surface the driving effect is related to the seasonal change in the insolation, over sea surface, the gradual reduction in the incident solar radiation with time competes with a surface albedo increase. The clear-sky ocean albedo is a function of θ_s, the solar zenith angle. The larger the value of θ_s, the larger the TOA albedo. Therefore, the clear-sky ocean albedo is actually dependent on the latitude and local solar time. The surface albedo increase over desert surface with grazing solar zenith angle being largely less efficient (e.g., Loeb et al., 2003), only a net decrease in the OLR is reported above desert surface. Also illustrated in Fig. 3 (panel A.1) is a
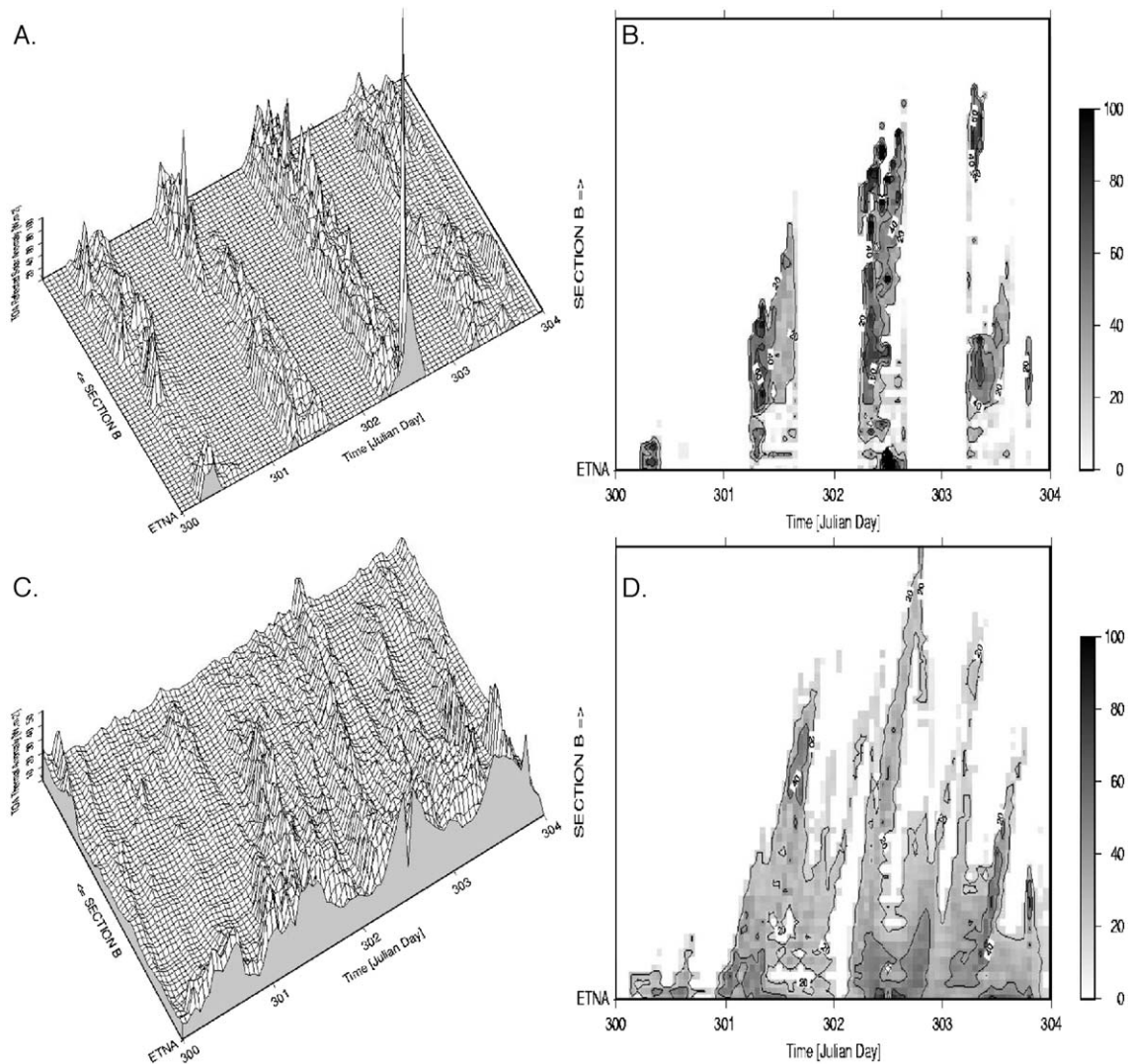

Fig. 5. Radiative perturbations along the section B (from the Etna location to 32.85°N, 16.01°E). Panels A and C provide, respectively, the anomalies in the reflected solar flux and emitted thermal radiation at the TOA from October 27 to October 30 with respect to a reference clear sky situation, while panels B and D only display the radiative forcings related to the Etna eruption cloud. The SW forcing is a negative radiative forcing, while the LW forcing is a positive one. Units are given in W m^{-2}.

possible shadow contamination of the clear-sky reflected solar flux. Such a contamination results from the projection of cloud structure on the local plane of the Earth with respect to a direction of incoming solar radiation (e.g., Simpson, Jin, et al., 2000). This may lead to an overestimation of the SW volcanic cloud forcing if contaminated fluxes are used as reference clear-sky fluxes. In the two examples of shadow contamination given panel A.1, a selection of these fluxes as reference fluxes will overestimate the SW forcing by about 10 W m^{-2}. Finally, panels A.2 and B.2 in Fig. 3 indicate that clear-sky OLR daily variations can also be detected over both surface types, with a larger magnitude over desert surface.

To reduce the uncertainty range in the volcanic cloud forcing quantification related to the clear-sky variation, we determined for each of the 192 available Meteosat-7 scenes from October 27 to 30 (192 = 48 scenes a day*4 days) a

corresponding reference clear-sky OSR and OLR image rather than 48 generic reference clear-sky images as previously done when estimating the unfiltered TOA thermal radiance anomalies. During daytime, the reference clear-sky fluxes have been estimated taking advantage of our cloud screening algorithm (Ipe et al., 2002). Indeed, rather than considering the reference clear-sky value as being for each pixel in a given scene the highest (lowest) reflected solar (emitted thermal) flux found in the 14 days time series, we selected as reference flux the closest (in day) clear-sky flux from the day for which the reference image has to be estimated. The cloud algorithm only uses visible narrow-band radiance measurement made by an imager to estimate the cloud optical depth and does not require to priorly flag cloudy pixels by some cloud detection scheme. Practically, the cloud optical thickness is related to measured visible
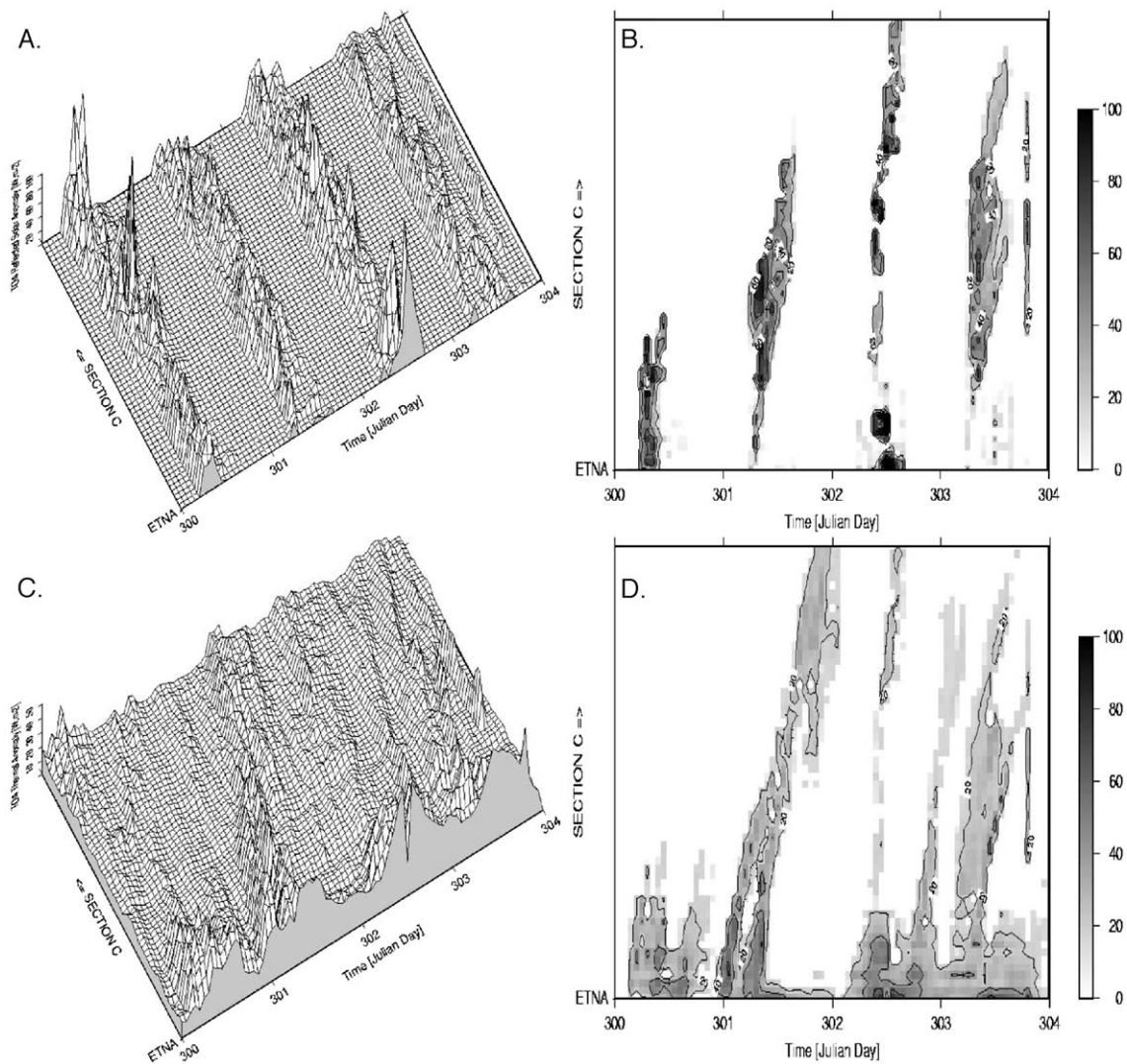

Fig. 6. Radiative perturbations along the section C (from the Etna location to 32.81°N, 15.26°E). Panels A and C provide, respectively, the anomalies in the reflected solar flux and emitted thermal radiation at the TOA from October 27 to October 30 with respect to a reference clear sky situation, while panels B and D only display the radiative forcing related to the Etna eruption cloud. The SW forcing is a negative radiative forcing, while the LW forcing is positive one. Units are given in W m^{-2}.
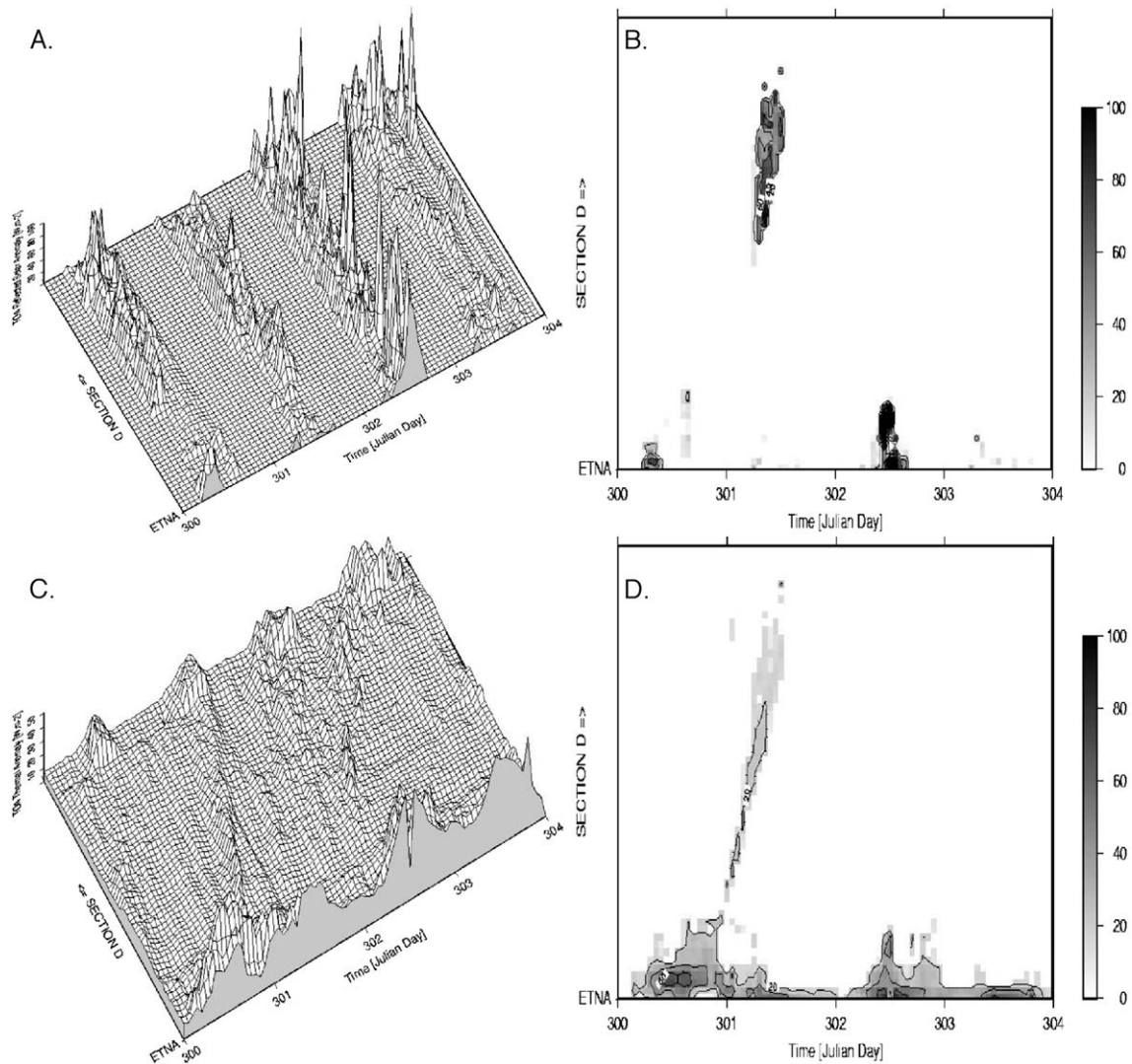
A.

B.

C.

D.

Fig. 7. Radiative perturbations along the section D (from the Etna location to 32.71°N, 11.39°E). Panels A and C provide, respectively, the anomalies in the reflected solar flux and emitted thermal radiation at the TOA from October 27 to October 30 with respect to a reference clear sky situation, while panels B and D only display the radiative perturbation related to the Etna eruption cloud. The SW forcing is a negative radiative forcing, while the LW forcing is a positive one. Units are given in W m^{-2}.

narrowband radiance using pre-computed look-up tables. The cloud fraction estimation is then based on cloudy imager pixels detection within some defined footprint; the cloudy test being simply a threshold on their associated cloud optical depth (further informations on our cloud algorithm are provided in Appendix A).

Finally, to minimise the risk of selecting cloud shadows and/or unscreened cloudy pixels the simple minimum/maximum value technique was adjusted with a condition that looks at the temporal trend in the OSR/OLR in each pixel during the compositing period. Namely, fluxes larger or lower than $\bar{F} \pm \sigma$ with $\bar{F}$ the arithmetic mean and σ the standard deviation of the clear-sky flux time series relative to a given pixel and a given day time Meteosat scene, are removed from each clear-sky fluxes time series. Clearly, this is certainly not the most rigorous way to handle cloud shadow (see, e.g., Simpson & Sitt, 1998; Simpson, Jin, et

al., 2000); nevertheless, it allows a cloud shadow detection and removal at low CPU time cost well suited to the time constrain required by the operational Meteosat-7 data processing at RMIB. Because our cloud-screening algorithm has been developed to be applied on recorded visible radiance, the reference OLR image computations after sunset rely on the criterion of the higher flux.

4.2. Results

Figs. 4–8 display the time evolution (computed scene by scene from October 27 to October 30) of the TOA radiative perturbation for both the OSR and OLR with respect to a clear-sky situation along the five (A to E) sections given in Fig. 1. Note that panels A and C in these figures provide the temporal radiative perturbations regardless of their origins (e.g., meteorological and/or volcanic clouds) while panels B
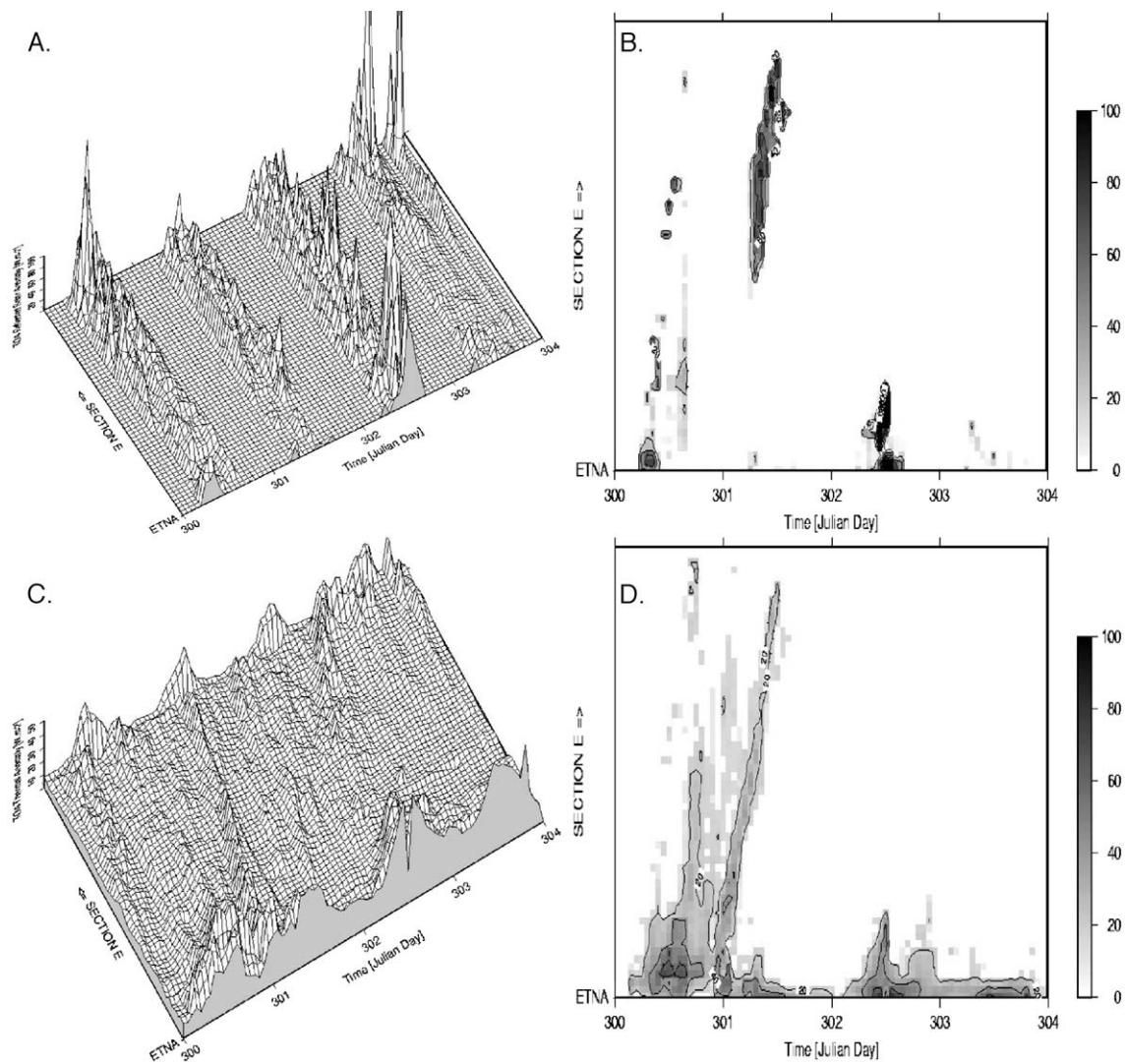
Fig. 8. Radiative perturbations along the section E (from the Etna location to 32.75°N, 12.77°E). Panels A and C provide, respectively, the anomalies in the reflected solar flux and emitted thermal radiation at the TOA from October 27 to October 30 with respect to a reference clear sky situation, while panels B and D only display the radiative forcings related to the Etna eruption cloud. The SW forcing is a negative radiative forcing, while the LW forcing is positive one. Units are given in W m^{-2}.

and D only give the radiative forcing (respectively SWECRF and LWECRF) introduced by the Etna eruption. Additionally, two animations (available at ftp://gerb.oma.be/cedric/) provide the time evolution of the TOA SWECRF (file Solar-F.gif) and LWECRF (file Therm-F.gif) over the region of study using data sampled at 1-h interval (units are given in W m^{-2}). As we see, during nighttime, both the incident and reflected solar radiation are null and the TOA radiative forcing only concerns the emitted thermal radiation. As for meteorological clouds, the volcanic cloud absorbs the infrared radiation and reduces the longwave radiation escaping to the space. This yields a warming with respect to clear skies and LWECRF is positive. Panel D in Figs. 4–8 reveals that this positive forcing reached up to 80 W m^{-2} on October 29.

As the day progresses, the Sun illuminates the Earth's surface and Figs. 4–8 as well as the animation, Solar-F.gif,

indicate a net OSR enhancement at TOA associated with the presence of the volcanic cloud in the atmosphere. While it is straightforward to understand why meteorological clouds reflect a significant amount of incoming solar radiation in regard to their high albedo in the visible, the situation can appear as more surprising in the case of a volcanic cloud. Due to the island location of the Mount Etna, the volcanic cloud originating from the volcano and stretched towards the north African coast appears to have a higher albedo in the solar spectrum than the underlying Mediterranean Sea. Therefore, the solar absorption by the surface is reduced due to the albedo effect, which results in a cooling in the shortwave energy budget with respect to clear skies. In addition, as the black graphite and carbon particles reduce the amount of sunlight reaching the planet's surface, they increase the amount of solar energy absorbed in the atmosphere, thus simultaneously cooling the surface and warming
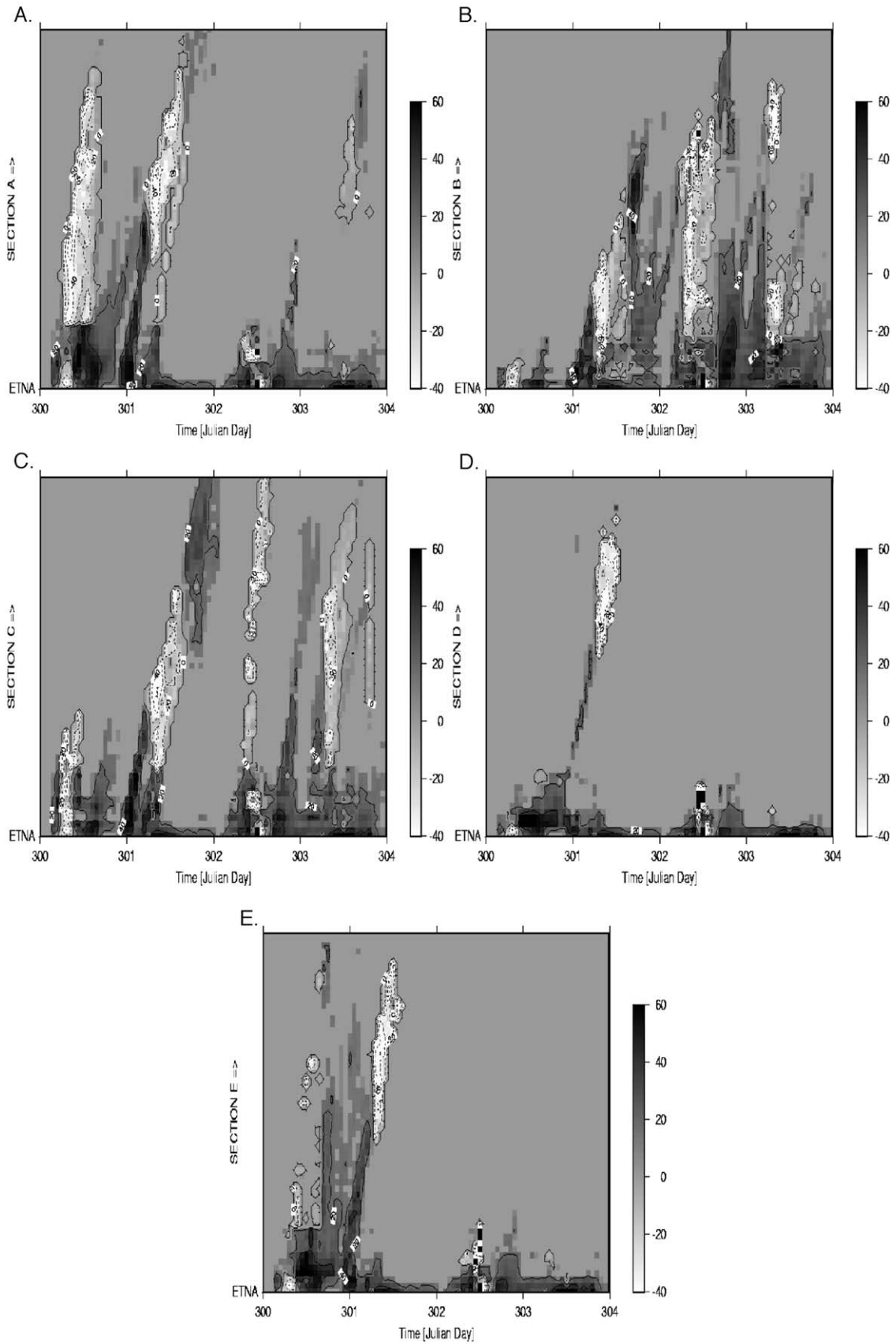
Fig. 9. Time evolution of the net volcanic cloud radiative forcing at the top of the atmosphere along the fives sections (A to E) defined in Fig. 1. Units are given in W m^{-2}.

the atmosphere. Hence SWECRF is negative. As indicated on panel B in Figs. 4–8, the SWECRF reached instantaneous values up to -230 W m^{-2} during the most explosive part of the October 29 (Julian day 302), 2002 eruption. (Instantaneous forcing values because they are obtained from satellite images during a specific overpass and time averaging has not been performed). Someone certainly noticed the extremely high SWECRF value displayed panel A in Fig. 5 on Julian day 302, namely -548 W m^{-2}. This value issues from a problem during the reception of the corresponding Meteosat-7 visible image and illustrates the absence of recorded visible radiance for this pixel.

When comparing the magnitude of the LW and SW volcanic cloud radiative forcings, we can note that while the absolute magnitude of the SWECRF appears as more than twice the magnitude of the LWECRF at the TOA, such a SW forcing magnitude does not significantly differ from the one generated by large meteorological clouds (as an example, see the SW forcing magnitude reported panel A in Fig. 6 at the end of section C on Julian day 300 and/ or the SW forcing reported panel A in Fig. 8 at the end of section E on Julian day 303). By contrast, panel C in Figs. 4–8 indicates that, while reduced with respect to the SW forcing, LW volcanic cloud forcing values are very discernible from the LW meteorological clouds forcing highlighting both the higher altitude of the volcanic cloud and the larger infrared absorption which takes place in such a cloud in comparison with meteorological clouds. Panels B and D in Figs. 4–8 also indicate that while the magnitude of the LWECRF shows a well observable decrease in the forcing's magnitude as the volcanic cloud move away from the Sicilian coast to the north African coast, such a decrease is largely less apparent for the SWECRF, which rather maintains a large negative forcing when crossing the Mediterranean Sea. Highest values of LWECRF close to the origin of the volcanic perturbation result from the fact that the largest silicate particles such as lapilli settle within hours following the eruption, which therefore reduce the atmospheric charge in absorbing material as the volcanic cloud stretch above the Mediterranean sea. In addition, already in the absence of any volcanic perturbation, the land/sea surface temperature contrast accounts for lower OLR above sea surface during daytime than above land surface. By contrast, the reduction in SW absorbing materials in the atmosphere combined with a lower Earth surface albedo values as the volcanic cloud escapes from the Sicilian coast acts to maintain high SWECRF values above the Sea.

Regarding the net radiative effect at the TOA, Fig. 9 indicates that NETECRF may be positive or negative depending on the time and the remoteness from the Mount Etna location. During nighttime, in the absence of solar radiation, the NETECRF is positive (warming) and the temporary large atmospheric loading can reduce the amplitude of the diurnal cycle of surface air temperature in the region of the tropospheric volcanic cloud. During daytime,

the NETECRF at the TOA is largely negative with instantaneous forcing values reaching up to about -185 W m^{-2} on October 29 (Julian day 302) when highly explosive eruption occurred. However, as highlighted in Figs. 4–8 panels B and D, the LWECRF exhibits a larger horizontal extend than the SWECRF does in the vicinity of the origin of the volcanic perturbation which can therefore induce a positive NETECRF at the TOA beside the main direction of the volcanic cloud. The temporal and spatial evolution of the NETECRF induced by the October 27 (Julian day 300) eruption well illustrates the occurrence of such positive NETECRF event. Indeed, Fig. 9 indicates that a negative NETECRF is retrieved at the origin of our five-section (A to E) lines as the Sun began to illumine the Earth's surface on that October 27. However, as the volcanic cloud progressed above the sea according to a preferential direction, only the NETECRF computed along the section line close to the main direction of propagation (section C) still showed a negative TOA net. NETECRF, estimated along the other directions (e.g., sections A, B, D, and E), are null or positive. Fig. 9 indicates that such a positive net forcing can reach up to 70 W m^{-2} in the neighborhood of the Mount Etna location. Finally, a net negative forcing only recovered with a change in the main volcanic cloud direction of stretching (see the NETECRF evolution along the section A in Fig. 9).

5. Final remarks and conclusion

The volcanic cloud originating from the end of October 2002 Mount Etna eruption has been identified and tracked during the first 4 days of the eruption in order to estimate its induced radiative perturbations at the top of the atmosphere. The thermal bands' subtraction technique is commonly used to enhance the visibility of eruption clouds and discriminate them from meteorological cloud (e.g., Schneider et al., 1995). This method has significant limitations (see Simpson, Hufford, et al., 2000, 2002). In this study, we have used half-hourly Meteosat-7 visible, infrared (1 channel), and water vapor imagery, partly because Meteosat-7 does not have the two thermal infrared channels, required by the split window method of volcanic ash detection. Thanks to the temporal and spatial resolution of the Meteosat sensor allowed by its geostationary orbit; it was possible after an unfiltering of the Meteosat-7 measurements to identify and track the eruption cloud from the Mount Etna location to the north African coast by computing longwave thermal radiance anomalies at the top of the atmosphere over the geographical area of interest. It is important to note that the approach developed herein assumes that a representative background clear-sky reference state case can be defined. While in the present study the conditions of our assumption to create reference images appear to be met, due to the related location and seasonal issues as well as mete-

orological conditions it could be much less likely in other situations. In addition, the high temporal sampling of the study area by the Meteosat-7 sensor has ensured us that airborne dust from distant regions (e.g., Gobi and Sahara) had not contributed to a false volcanic ash signal, which could appear in case of violent sand storms (see Simpson, Hufford, Servranckx, Berg, & Pieri, 2003 for a discussion of the false volcanic ash signal produced by fine grain airborne Saharan or Gobi dust in thermal infrared differ-ence imagery). Then, by performing angular conversion on both directional solar and thermal radiance to deter-mine the broadband unfiltered fluxes at the top of the atmosphere, it was possible to estimate the shortwave, longwave, and net radiative forcing at the top TOA on a half-hour basis induced by the introduction of the volcanic cloud in a previously clear sky.

Our results indicate that, as for meteorological clouds, the volcanic eruption cloud presents a negative shortwave forcing and a positive longwave forcing at the TOA. The net effect may be positive or negative depending on the time and the distance from the origin of the volcanic perturbation. Nevertheless, these results could be volcano-dependent especially in the shortwave where the difference between the volcanic cloud albedo and the underlying surface albedo could be quite different for a fully continental volcano. Regarding the amplitude of the forcings, we have shown that, while the Etna volcanic cloud has introduced a well-discernable radiative perturbation with respect to a clear-sky situation, the SW volcanic cloud forcing appears in the range of the one introduced by large clouds above the Mediterranean Sea. By contrast, the perturbation generated in the LW spectrum at the TOA, while lower in absolute term than in the SW part of the spectrum, is larger than the one introduced by large meteorological clouds. The magni-tude of this LW forcing (which is directly related to the volumes of silicate material injected in the atmosphere and to the altitude of the volcanic cloud) is open to grow if, as suggested by Schiano, Clocchiatti, and Ottolini (2001), the Mount Etna volcano is undergoing a gradual shift to become an "island arc" volcano and thus a more explosive and unpredictable volcano.

Finally, the successful launch of Meteosat Second Generation (MSG-1) last summer (August 2002) will allow us to improve our detection and radiative monitoring of the forthcoming Mount Etna eruptions by a combined use of data originating from its two instruments. The Spinning Enhanced Visible and Infrared Imager (SEVIRI) (Schmetz et al., 2002) is a new imager with improved spectral resolution (12 channels). It allows a better identification and tracking of the volcanic plume and eruption cloud by a combined use of the split window differencing technique of thermal longwave infrared channels and the longwave thermal radiance anomalies approach. Moreover, the Geo-stationary Earth Radiation Budget (GERB) (Harries & Crommelynck, 1999) instrument will provide accurate broadband measurements of the radiant energy at the TOA and thus a better estimation of the volcanic cloud forcing.

Appendix A. Overview of the RMIB operational cloud screening algorithm

As shown in Nakajima and Nakajima (1995), there is an empirical law between the visible radiance, thus reflec-tance, and the cloud optical depth, which is nearly insen-sitive to the cloud particle size, r, for visible wavelengths. By introducing the mean cloud amount (or cloud coverage index), C, defined as (Cano et al., 1986):

$$C(\theta_s, \theta_v, \phi, \text{surface}, \text{phase}, \tau)$$
$$= \frac{L(\theta_s, \theta_v, \phi, \text{surface}, \text{phase}, \tau) - L(\theta_s, \theta_v, \phi, \text{surface}, \tau = 0)}{L(\theta_s, \theta_v, \phi, \text{phase}, \tau = 128) - L(\theta_s, \theta_v, \phi, \text{surface}, \tau = 0)}$$
(12)

where $\tau = 0$ represents clear-sky conditions above the ground surface, $\tau = 128$ denotes the opposite boundary limit associated with optically opaque cloudy conditions leading to simulated radiance fields insensitive to surface albedo; this law is simply rescaled with C values ranging from 0 to 1. This empirical law has been built by running the Streamer RT code (Key, 2001). Note that we have used built-in Lambertian spectral response curves for desert (sand) and vegetation, which do not allow us to take into account complex angular scene signatures such as the hot spot effect for vegetation. The most noticeable fact when plotting this law according to the optical depth is its similar shape for all scene viewing geometries as it is illustrated in Fig. 10. Note that the curve is not saturated at $C = 1$ when $\tau = 128$ due to the fact that the reflection function of the optically opaque clouds generated by the radiative transfer code is still increasing with the cloud optical depth. This simply occurs because the upper boundary conditions $\tau = 128$ for $C = 1$ were fixed to agree with the CERES cloud properties retrievals ($\tau \leq 128$), while saturation is only reached for $\tau \approx 400$ in the radiances simulated by run-ning the Streamer model.

Due to the characteristic shape of the function, we parameterized this relation by using a modified sigmoid function of the logarithm of the optical depth (the C values larger than 1 were also considered when the fit on the look-
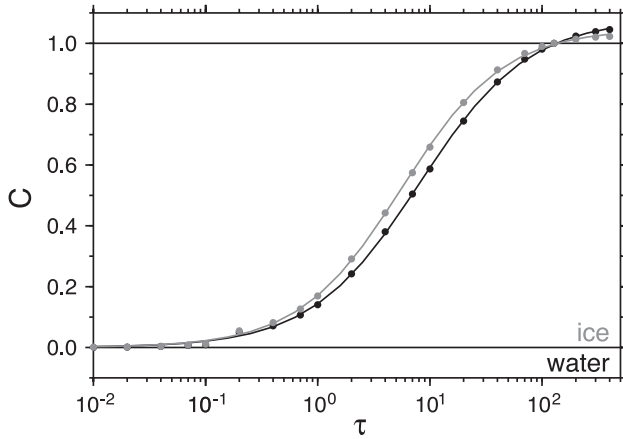
Fig. 10. Mean cloud amount C versus cloud optical depth τ empirical curves for ocean under single layer and homogene water and ice clouds using the STREAMER RT code (bullets). The plain curves give the least square fit using our modified sigmoid on these RT values. The scene geometry is $\theta_s = 30°$, $\theta_v = 60°$ and $\phi = 0°$.

up table curves was performed). It must be noted that the sigmoid function of the optical depth does not satisfy mathematically the boundary value problem of $C = 0$ for $\tau = 0$. However, it is asymptotically satisfied ($C \overset{\tau \to 0}{\to} 0$) for $C = f(\log \tau)$, where f is defined as

$$f(\log \tau) = \frac{A}{B + 10^{-(\log \tau - \log \tau_0)/\chi}}$$

with the use of four parameters (A, B, $\tau_0 > 0$, and $\chi \neq 0$). In the latter expression, the dependency of C and of the four parameters with the scene viewing geometry (θ_s, θ_v, ϕ), ground surface and cloud phase is implicitly assumed. Some basic algebra leads us to the compact form

$$C = \frac{A}{B + \left(\frac{\tau_0}{\tau}\right)^{1/\chi}} \qquad (13)$$

These four parameters can then be adjusted in order to get the closest match between the empirical curve and our modified sigmoid through a least square fit on the RT data. Practically, we choose the Powell multidimensional fitting method as described in Press, Vetterling, Tseukolsky, and Flannery (1992). Finally, we end up with a set of four parameters for each scene viewing geometry, surface, and cloud phase instead of twice (C and τ) the number of optical depth values. Moreover, this continuous relation between C and τ can be seen as an implicit non-linear interpolation on the discrete τ and C values computed by the RT code, while standard cloud optical depth retrieval methods are linearly interpolating between the nearest values. We can directly see the benefit of the simple formulation of our fitting function. Indeed, we can explicitly solve Eq. (13) for the cloud optical depth, leading us to

$$\tau = \frac{\tau_0 \cdot C^\chi}{(A - B \cdot C)^\chi} \qquad (14)$$

with the mathematical constraints of Eq. (13) ($\chi \neq 0$, $\tau_0 > 0$) and setting the retrieved τ value to 128 when $C \geq A/B$ or $C \geq 1$ (saturation condition).

Thus, our cloud optical thickness retrieval algorithm immediately follows. For each imager pixel:

(1) We estimate its cloud phase, no matter what it is cloudy or not.
(2) We compute its associated mean cloud amount value, C, using Eq. (12), where the clear-sky radiance, $L(\theta_s, \theta_v, \phi, surface, \tau = 0)$, above the same pixel is extracted from some statistical algorithm (Ipe, Bertrand, Clerbaux, Dewitte, & Gonzalez, accepted), the optically opaque cloudy radiance, $L(\theta_s, \theta_v, \phi, phase, \tau = 128)$, is the RT simulated value for the associated pixel's viewing geometry (θ_s, θ_v, ϕ) and ground surface.
(3) We compute its associated cloud optical depth value using Eq. (14) and the four fitted parameters for the associated pixel's viewing geometry, ground surface, and cloud phase.

This final value as well as the optically opaque cloudy radiance is obtained by tri-linear interpolations on the associated values of the nearest $2 \times 2 \times 2$ angles to (θ_s, θ_v, ϕ). Finally, according to its associated cloud optical depth, the pixel is flagged cloudy if $\tau > \tau_{thres}$. Comparisons of this cloud optical depth retrieval scheme with other literature algorithms have shown that a value of $\tau_{thres} = 0.6$ gives the best matches.

As we previously stated in the text, this simple (due to operational constraints) method was developed to provide cloud properties estimates as close as possible to the CERES retrievals in order to minimize errors in the ADM selection process. Therefore, rather than validate our algorithm against observed (spectrophotonic) measurements of optical thickness and in situ (LIDAR) observations of clouds, the validation was performed against the CERES algorithm (Minnis et al., 1995) by comparing retrievals for collocated measurements of CERES and Meteosat-7.

References

Belward, A. S. (Ed.) (1996). The IGBP-DIS global 1 km land cover data set (DISCover)—proposal and implementation plans. IGBP-DIS Working Paper No. 13, Toulouse, France. 61 pp.

Belward, A. S., Estes, J. E., & Kline, K. D. (1999). The IGBP-DIS 1-km Land-Cover Data Set DISCover: A project overview. Photogrammetric Engineering and Remote Sensing, 65(9), 1013–1020.

Bertrand, C., van Ypersele, J. -P., & Berger, A. (1999). Volcanic and solar impacts on climate since 1700. Climate Dynamics, 15, 355–367.

Bertrand, C., van Ypersele, J. -P., & Berger, A. (2002). Are natural climate forcings able to counteract the projected anthropogenic global warming? Climatic Change, 55, 413–427.

Cano, D., Monget, J. M., Albuisson, M., Guillard, H., Regas, N., & Wald, L. (1986). A method for the determination of the global solar radiation from meteorological satellite data. Solar Energy, 37, 31–39.

Casadevall, T. J. (1994). Perspectives on the hazards of volcanic ash.

First International Symposium on Volcanic Ash and Aviation Safety. *U.S. Geol. Survey Bull., vol. 2047* (pp. 1–6). Washington, DC: Geological Survey.

Casadevall, T. J., & Krohn, M. D. (1995). Effects of the 1992 Crater Peak eruptions on airports and aviation operations in the United States and Canada. *U.S. Geol. Survey Bull., 2139*, 205–220.

Clerbaux, N. (2002). Meteosat Count versus CERES-TRMM Unfiltered Radiance. RMIB GERB Technical Note *MSG-RMIB-GE-TN-0036*, Brussels. 4 pp.

Clerbaux, N., Dewitte, S., Gonzalez, L., Bertrand, C., Nicula, B., & Ipe, A. (2003). Outgoing longwave flux estimation: Improvement of angular modeling using spectral information. *Remote Sensing of Environment, 85*, 389–395.

Dewitte, S., & Clerbaux, N. (1999). First experience with GERB ground segment processing software: Validation with CERES PFM data. *Advance in Space Research, 24*(7), 925–929.

Hansen, J. E., Wang, W. C., & Lacis, A. A. (1978). Mount Agung provides a test of global climatic perturbation. *Science, 199*, 1065–1068.

Harries, J. E., & Crommelynck, D. (1999). The geostationary earth radiation budget experiment on MSG-1 and its potential applications. *Advance in Space Research, 24*, 915–919.

Hartmann, D. L., Moy, L. A., & Fu, Q. (2001). Tropical convection and energy balance at the top of the atmosphere. *Journal of Climate, 14*, 4495–4511.

Hirono, M., Shibata, T., & Fujiwara, M. (1985). A possible relationship of volcanic aerosol variations with El Niño Southern Oscillations–Lidar observations of volcanic aerosols in the atmosphere. *Journal of the Meteorological Society of Japan, 63*, 303–310.

Holben, B.N. (1986). Characteristics of maximum-value composite images from temporal AVHRR data. *International Journal of Remote Sensing, 7*, 1417–1434.

Ipe, A., Bertrand, C., Clerbaux, N., Dewitte, S., & Gonzalez, L. (2003). Pixelscale composite TOA clear-sky reflectances for Meteosat-7 visible data. *Journal of Geophysical Research* (accepted).

Ipe, A., Bertrand, C., Clerbaux, N., Dewitte, S., Gonzalez, L., & Nicula, B. (2002). Validation and homogenization of the cloud properties retrievals for RMIB GERB/SEVIRI scene identification. In K. P. Schäfer, O. Lado-Bordowsky, A. D. Comerón, & R. H. Picard (Eds.), *Remote sensing of clouds and the atmosphere VII. SPIE Proceedings Series, vol. 4882* (pp. 29–39).

Key, J. R. (2001). *Streamer (version 3.0) user's guide*. Madison, WI, USA: NOAA/NESDIS, 106 pp.

Loeb, N. G., Smith, N. M., Kato, S., Miller, W. F., Gupta, S. K., Minnis, P., & Wielicki, B. A. (2003). Angular distribution models for top-of-atmosphere radiative flux estimation from the clouds and the earth's radiant energy system instrument on the tropical rainfall measuring mission satellite: Part 1. Methodology. *Journal of Applied Meteorology, 42*, 240–265.

Minnis, P., Kratz, D. P., Coakley Jr., J. A., King, M. D., Garber, D., Heck, P., Mayor, S., Young, D. F., & Arduini, R. (1995). Cloud optical property retrieval (subsystem 4.3). In CERES Science Team (Ed.), *Clouds and the Earth's Radiant Energy System (CERES) Algorithm Theoretical Basis Document: Volume III. Cloud Analyses and Radiance Inversions (Subsystem 4). NASA RP 1376, vol. 3* (pp. 135–176).

Nakajima, T. Y., & Nakajima, T. (1995). Wide-area determination of cloud microphysical properties from NOAA AVHRR measurements for FIRE and ASTEX regions. *Journal of the Atmospheric Sciences, 52*, 4043–4059.

Pieri, D., Ma, C., Simpson, J. J., Hufford, G., Grindle, T., & Grove, C. (2002). Analyses of in-situ airborne volcanic ash from the February 2000 eruption of Hekla Volcano, Iceland. *Geophysical Research Letters, 29*, 19-1–19-4.

Prata, A. J. (1989). Infrared radiative transfer calculations for volcanic ash clouds. *Geophysical Research Letters, 16*, 1293–1296.

Press, W. H., Vetterling, W. T., Teukolsky, S. A., & Flannery, B. P. (1992). Numerical recipes in C. *The art of scientific computing* (2nd ed.). Cambridge: Cambridge Univ. Press.

Ramanathan, V., Cess, R. D., Harrison, E. F., Minnis, P., Barkstrom, B. R., Ahmad, E., & Hartmann, D. (1989). Cloud-radiative forcing and climate: Results from the earth radiation budget experiment. *Science, 243*, 57–63.

Rampino, M. R., & Self, S. (1984). Sulphur-rich volcanic eruptions and stratospheric aerosols. *Nature, 310*, 677–679.

Richiazzi, P., Yang, S., Gautier, C., & Sowle, D. (1998). SBDART: A research and teaching software tool for plane-parallel radiative transfer in the earth's atmosphere. *Bulletin of the American Meteorological Society, 79*, 2101–2114 (Available at http://arm.mrcsb.com/sbdart).

Robock, A., & Mao, J. (1995). The volcanic signal in surface temperature observations. *Journal of Climate, 8*, 1086–1103.

Robock, A., & Matson, M. (1983). Circumglobal transport of the El Chichón volcanic dust cloud. *Science, 221*, 195–197.

Rose, W. I. (1986). Interaction of aircraft and explosive eruption clouds: A volcanologist's perspective. *AIAA Journal, 25*, 52–58.

Schiano, P., Clocchiatti, R., & Ottolini, L. (2001). Transition of Mount Etna lavas from a mantle plume to an island-arc magmatic source. *Nature, 412*, 900–904.

Schmetz, J., & Liu, Q. (1988). Outgoing longwave radiation and its diurnal variation at regional scales derived from Meteosat. *Journal of Geophysical Research, 93*, 11192–11204.

Schmetz, J., Pili, P., Tjemkes, S., Just, D., Kerkmann, J., Rota, S., & Ratier, A. (2002). An introduction to Meteosat Second Generation (MSG). *Bulletin of the American Meteorological Society, 83*, 977–992.

Schneider, D. J., Rose, W. I., & Kelley, L. (1995). Tracking of 1992 eruption clouds from Crater Peak Vent of Mount Spurr Volcano, Alaska, using AVHRR. In T. E. C. Keith (Ed.), *The 1992 Eruptions of Crater Peak Vent, Mount Spurr Volcano, Alaska. U.S. Geological Survey Bull., vol. B-2139* (pp. 27–36).

Simpson, J. J., Hufford, G. L., Pieri, D., & Berg, J. S. (2000). Failures in detecting volcanic ash from a satellite-based technique. *Remote Sensing of Environment, 72*, 191–217.

Simpson, J. J., Hufford, G. L., Pieri, D., Servranckx, R., Berg, J. S., & Bauer, C. (2002). The February 2001 eruption of Mount Cleveland, Alaska: Case study of an Aviation Hazard. *Weather and Forecasting, 17*, 691–704.

Simpson, J. J., Hufford, G. L., Servranckx, R., Berg, J. S., & Pieri, D. (2003). Airborne Asian dust: Case study of long-range transport and implications for the detection of volcanic ash. *Weather and Forecasting, 18*, 121–141.

Simpson, J. J., Jin, Z., & Stitt, J. R. (2000). Cloud shadow detection under arbitrary viewing and illumination conditions. *IEEE Transactions on Geoscience and Remote Sensing, 38*, 972–976.

Simpson, J. J., & Sitt, J. R. (1998). A procedure for the detection and removal of cloud shadow from AVHRR data over land. *IEEE Transactions on Geoscience and Remote Sensing, 36*, 880–897.

Stenchikov, G. L., Kirchner, I., Robock, A., Graf, H. -F., Antuña, J. C., Grainger, R. G., Lambert, A., & Thomason, L. (1998). Radiative forcing from the 1991 Mount Pinatubo volcanic eruption. *Journal of Geophysical Research, 103*, 13837–13857.

Wen, S., & Rose, W. I. (1994). Retrieval of sizes and total masses of particles in volcanic clouds using AVHRR bands 4 and 5. *Geophysical Research Letters, 99*, 5421–5431.

Wielicki, B. A., Barkstroöm, B. R., Harrison, E. F., Lee III, R. B., Smith, G. L., & Cooper, J. E. (1996). Clouds and the earth's radiant energy system (CERES): An earth observing system experiment. *Bulletin of the American Meteorological Society, 77*, 853–868.

Yamanouchi, T., Suzuki, K., & Kawaguchi, S. (1989). Detection of clouds in Antarctica from infrared multispectral data of AVHRR. *Journal of the Meteorological Society of Japan, 65*, 949–962.